International Journal of Hyperthermia

ISSN: (Print) (Online) Journal homepage: https://www.tandfonline.com/loi/ihyt20

Predictions of optimal heating by magnetic reversal behavior of magnetic nanowires (MNWs) with different materials

Yicong Chen & Bethanie J.H. Stadler

To cite this article: Yicong Chen & Bethanie J.H. Stadler (2023) Predictions of optimal heating by magnetic reversal behavior of magnetic nanowires (MNWs) with different materials, International Journal of Hyperthermia, 40:1, 2223371, DOI: 10.1080/02656736.2023.2223371

To link to this article: https://doi.org/10.1080/02656736.2023.2223371

INTERNATIONAL JOURNAL OF HYPERTHERMIA
2023, VOL. 40, NO. 1, 2223371
https://doi.org/10.1080/02656736.2023.2223371

Predictions of optimal heating by magnetic reversal behavior of magnetic nanowires (MNWs) with different materials

Yicong Chen[a] and Bethanie J.H. Stadler[a,b]

[a]Department of Chemical Engineering and Material Science, University of Minnesota, Minneapolis, MN, USA; [b]Department of Electrical and Computer Engineering, University of Minnesota, Minneapolis, MN, USA

ABSTRACT

Objective: Magnetic nanowires (MNWs) are potential candidates for heating in biomedical applications that require rapid and uniform heating rates, such as warming cryopreserved organs and hyperthermia treatment of cancer cells. Therefore, it is essential to determine which materials and geometries will provide the optimal heating using available alternating magnetic fields (AMF).

Method: Micromagnetic simulations are used to investigate the heating ability of MNWs by predicting their hysteretic behavior. MNWs composed of iron (Fe), nickel (Ni), cobalt (Co) or permalloy (FeNi alloy, Py) with different diameters (10-200 nm) are simulated using object oriented micromagnetic framework (OOMMF).

Results: Hysteresis loops are obtained for each simulated MNW, and the 2D/3D magnetic moment map is simulated to show the reversal mechanism. The heating ability, in terms of specific loss power (SLP), is calculated from the area of the hysteresis loop times frequency for each MNW for comparison with others.

Conclusion: It is estimated that a theoretical optimal heating ability of 2730 W/g can be provided by isolated Co MNWs with 50 nm diameters using a typical AMF system that can supply 72 kA/m field amplitude and 50 kHz in frequency. Generalized correlation between coercivity and size/material of MNWs is provided as a guidance for researchers to choose the most appropriate MNW as a heater for their AMF system and *vice versa*.

ARTICLE HISTORY
Received 8 February 2023
Revised 17 May 2023
Accepted 5 June 2023

KEYWORDS
Magnetic nanowires; micromagnetic simulation; nanowarming; modeling (i.e., heat transfer, ultrasound, EM, integrated, treatment planning)

Introduction

Magnetic nanowires (MNWs) are one-dimensional magnetic nanomaterials with large magnetic anisotropies resulting from their high aspect ratios. MNWs have been employed in a variety of fields, including data storage devices *via* the giant magnetoresistance (GMR) effect [1–4], magnetic resonance imaging (MRI) contrast agents [5], bio-barcoding [6–7], and heating sources in biomedical applications, such as hyperthermia treatment for cancer cells and nanowarming for cryopreserved organs [8–11].

Applications related to heating have triggered the exploration of magnetic reversal behaviors in MNWs under alternating magnetic fields (AMF), where inductive losses are dissipated as heat [12–13]. Especially in nanowarming applications, fast heating is required because cryopreservation agents (CPAs) will devitrify if they are warmed slowly [14]. A variety of magnetic nanomaterials with different shapes and/or materials have been studied while researchers seek optimal biomedical heating [15–18]. Serantes et.al. suggested that optimized heating of spherical magnetic nanoparticles can be obtained when the particles are aligned as chains in the direction of the externally applied magnetic field [19–21]. MNWs are magnetically similar to chained spherical particles where the shape dictates the performance. Specifically, heating ability (widely referred to as specific loss power, SLP) is optimized when the external field is applied in the direction parallel to the long axis [21], which is the configuration that provides the largest hysteresis loop area. Similarly, Das et al. compared the heating ability of nanoparticles with different shapes, and they found that cylindrical particles with high aspect ratios and parallel external fields have the best heating ability [22]. To date, only limited shapes and materials have been studied experimentally [9,23,24]. Recall that the area of a hysteresis loop has units of Joules per gram, which is Watts per gram if multiplied by frequency (moment x field x frequency = J/g × Hz = W/g).

From the simulation results in this study, it is observed that the hysteresis loops of MNWs can be rectangular at the frequencies available in typical AMF heaters, and the width of this loop is wholly dependent on the MNW diameter. It is well known that rectangular loops enable scientists to reach the theoretical maximum heating limit ($M_{saturation}$ × field) for the given material and field strength [25]. This makes MNWs

CONTACT Yicong Chen chen6587@umn.edu Department of Chemical Engineering and Material Science, University of Minnesota, Minneapolis, MN, USA
Supplemental data for this article can be accessed online at https://doi.org/10.1080/02656736.2023.2223371.

a viable candidate for heating applications, and it is essential to study the factors that affect the shapes and widths of their hysteresis loops.

Theoretically, if the diameter of an MNW is smaller than the material-specified critical diameter $D_c = 5.208\sqrt{\frac{2A}{\mu_0 M_s^2}}$, transverse domain walls or coherent rotation will be the likely reversal mechanism [26]. Here A is the exchange parameter, μ_o is the permeability of free space, and M_s is the saturation magnetization. This critical diameter describes the size boundary between ferromagnetic alignment along the MNW length and vortex formation where the flat end of the MNW enables moments to lie in-plane so switching occurs *via* the propagation of this vortex as a domain wall. When the diameter is above the critical diameter, the magnetic moment can curl into vortices during the switching process, often as vortex walls [27–28]. In some cases, the Dzhyaloshinskii-Moriya interaction (DMI) within the MNW, also known as the antisymmetric exchange, can lead to skyrmion lines along with a stable 3D hedgehog state/Bloch point at the center of the MNW [29–31]. While this magnetic state is interesting for other applications, such as computing, it will, unfortunately, reduce the heating ability of MNWs and is therefore not desirable in this study. Here, we study how the reversal mechanism of different materials and diameters will impact the hysteresis loops, and we will use this information to predict the heating performance of isolated MNWs.

The magnetic reversal behavior of large MNW arrays can be easily measured by a vibrating-sample magnetometer (VSM). However, when it comes to the characterization of small arrays or isolated MNWs, more precise and expensive techniques such as superconducting quantum interference device (SQUID) [32] and high-resolution magneto-optical Kerr effect (MOKE) microscopy will be needed [33]. Micromagnetic simulations serve as a good substitute to study the magnetic properties of individual MNW or small arrays of MNWs without cost and time.

Method

Micromagnetic simulation *via* the publicly available code OOMMF is performed in this research [34]. In this simulator, a finite difference simulation is carried out. Effective field H_{eff} is recognized by the simulator, which integrates the externally applied field with the demagnetization, anisotropy, and exchange fields. The magnetization at each applied H_{eff} is determined by minimizing the system energy at that field. The dynamics of the magnetic moment during the reversal process are obtained by solving the Landau–Lifshitz-Gilbert (LLG) Eq. (1):

$$\frac{dM}{dt} = -|\bar{\gamma}|\mathrm{M} \times \mathrm{H}_{eff} - \frac{\alpha|\bar{\gamma}|}{\mathrm{M_s}}\mathrm{M} \times (\mathrm{M} \times \mathrm{H}_{eff}) \quad (1)$$

where $\bar{\gamma}$ is the gyromagnetic ratio and α is the damping factor. The first part of Equation (1) is the processional dynamics of a system and the second part accounts for the damping dynamics [35]. In this study, low frequency is assumed which means there is little dependence on the damping factor ($\alpha = 0.5$). The input of the micromagnetic simulation *via* OOMMF can be categorized into three parts: the geometry parameter, the material-specified parameter and the evolver type. In terms of the geometry parameters in this study, cylinders with a fixed length of 3 μm and varying diameters from 10 to 200 nm are used to represent the MNWs. In each simulation, the cylinders are geometrically subdivided into a rectangular mesh made up of cells. The length of each cell in the direction of the long axis of the cylinder is 60 nm (corresponding to 50 cells along this direction). In the other two directions, there are ~20 cells for each MNW with the side length depending on the diameter of the nanowire (for example, MNW with 50 nm diameter corresponds to a cell size of 2.5 nm × 2.5 nm in the plane perpendicular to the long axis of MNW). Figure 1(a) shows the generalized geometry of an MNW, as well as the resulting magnetic moment map obtained from the simulation.

Different values of A and M_s are used to account for different materials composing the MNWs (Table 1). Key parameters such as shape anisotropy (K_m) and critical diameter (D_c) are calculated for each material.

A polycrystalline morphology is assumed in this simulation for all MNWs, which means the crystalline anisotropy (K_c) will be negligible compared to the shape anisotropy of MNWs. The crystalline anisotropy energy in all of the materials studied here is at least 100 times less than the magnetostatic (shape) energy density of nano-cylinders, which is $2\pi M_s^2$ [37] for cubic Co, Ni, Fe, Py (10^6–10^7 J/m^3 at room temperature). The inductive loss that can be generated by each isolated MNW is characterized by the area enclosed by the simulated hysteresis loops as mentioned above.

The evolver used in this simulation series is the minimization evolver. Energy minimization is carried out at each externally applied field (sweeping between positive and negative saturation of MNW) to find out the magnetic moment state of MNWs when the system reaches an equilibrium. The direction notation of the applied field and the resulting magnetic moment represented by arrows can be found in Figure 1 (b). As a result, hysteresis loop can be obtained with the output magnetization and the 2D/3D

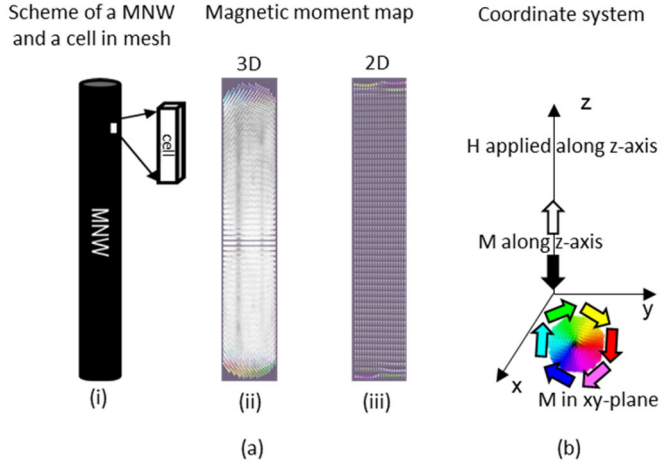

Figure 1. The generalized simulation scheme: (a) Geometry of an MNW and the resulting magnetic moment map, where (i) shows the basic shape information of an MNW and a cell, (ii) and (iii) gives an example of resulting magnetic moment map in 3D and 2D respectively; (b) The coordinate system including direction of applied field H and color-coded directions for the magnetic moment.

Table 1. Exchange parameter (A), saturation magnetization (M_s), shape anisotropy (K_m) and critical diameter (D_c) specified for different materials used in this study.

Materials	Exchange Parameter [A in (J/m)] [36]	Saturation Magnetization [M_s in (kA/m)] [28]	Shape Anisotropy [K_m in (J/m^3)]	Critical diameter [D_c in nm]
Co	1.30×10^{-11}	1398	1.8×10^7	17.0
Fe	0.81×10^{-11}	1700	1.2×10^7	11.0
Ni	0.34×10^{-11}	485	1.5×10^6	25.0
Py	1.05×10^{-11}	798	4.0×10^6	26.7

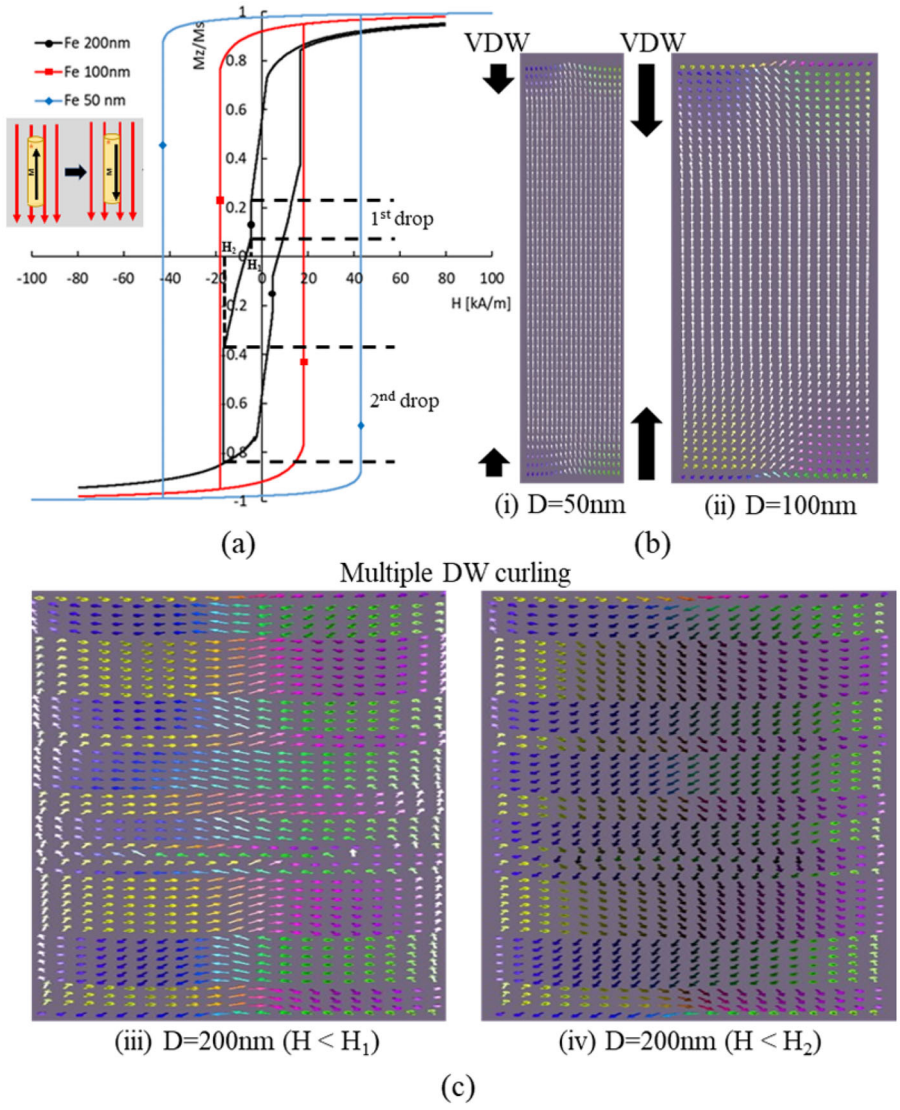

Figure 2. (a) Hysteresis loops of Fe MNWs with diameters of 50 nm (blue with diamond), 100 nm (red with square) and 200 nm (black with dot) showing the inverse relationship between loop area and MNW size. The inlet figure on the left shows how the external field (red) switches the moment(black) within an MNW. (b) 2D snapshots of the magnetic moments at fields just smaller than the coercivity of Fe MNWs with (i) 50 nm diameter and (ii) 100 nm diameter. The black arrow indicates the length of the vortex domain walls. (c) 2D snapshots of the magnetic moments of the Fe MNW with 200 nm diameter at (iii) $H < H_1$ before the curling cores switch down and (iv) $H < H_2$ before the curling 'shells' switch down. [Note: aspect ratios in 2D snapshots are not to scale for easier visualization].

magnetic moment state can be recorded at each equilibrium state.

Results and discussions

The hysteresis loops of MNWs with different materials and sizes are simulated in this study. As a general trend, MNWs of the same material with larger diameters had smaller coercivities (H_c) and smaller remanent magnetizations (M_r), and this led to less area enclosed by the loops. Therefore, smaller MNWs are better at heating, and in nanowarming, they could also be better dispersed in CPA, such as glycerol and VS55 [38]. Similar trends are observed for all of the materials in this study, and the hysteresis loops of Fe MNWs are shown in (Figure 2(a)) as an example. Complete comparisons for MNWs of all sizes and materials are included in the supporting information (Figure S1).

Importantly, vortex domain walls (VDWs) are formed at the ends of Fe MNWs with 50 nm and 100 nm diameters during reversal, illustrated by colored arrows which represent in-

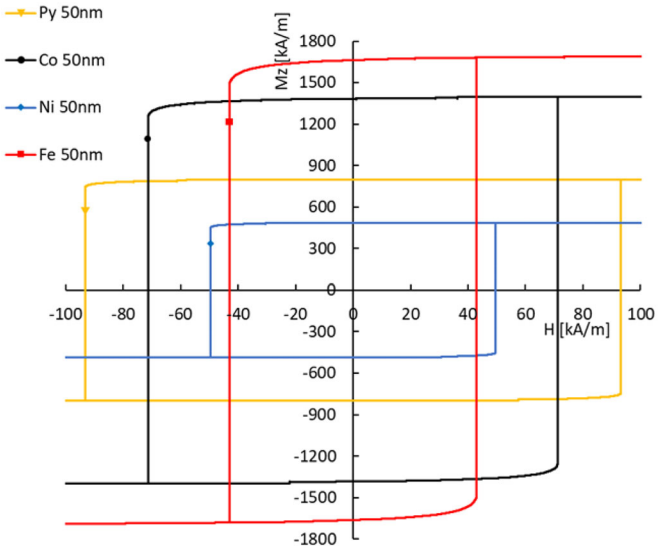

Figure 3. Hysteresis loops (using magnetization in z direction, M_z in [kA/m]) of Py (yellow with triangle), Co (black with dot), Ni (blue with diamond) and Fe (red with square) MNW with a diameter of 50 nm.

plane magnetic moments (Figure 2 (b(i) and (ii))). With increasing MNW diameter, the VDWs extend further down the MNW length before breaking away from the ends and propagating toward each other to fully switch the MNW at a specific applied field. These longer VDWs account for the decreasing M_r and increasing moment loss in the direction of the applied field before switching.

Interestingly, a specially shaped (in the form similar to a wasp waist) loop is observed for the Fe MNW with 200 nm diameter due to the formation and curling of multiple domains, which further reduced the area of the loop (complete reversal process is included in the supporting information Video.S1). It is observed from the wasp-waisted loop that there are two large drops of the moment (labelled in Figure 2 (a)). At H_1, the cores of the curling domains switched down (Figure 2 (b) (iv)), accounting for the first drop. At H_2, the external 'shell' of the curling domains switched down, accounting for the second drop. As a result, the area enclosed by the hysteresis loop of this MNW is greatly reduced compared to an ideal rectangle. Therefore, the formation of the DW, and the type of DW, strongly impacted the area enclosed by the hysteresis loops and thus affect the predicted heating ability.

For all of the materials studied, the MNWs with a diameter of 50 nm had coercivities within the fields easily achieved by typical AMFs, and they had the largest area loops within this constraint. Therefore, the 50 nm MNWs were compared next. The M_s-included hysteresis loops are plotted in Figure 3, showing that the coercivities range from 43 to 93 kA/m. Upon comparison between Figure 3 and Table 1, it can be seen that the coercivity appears to scale with a factor of A/M_s which agrees with the mechanism of vortex formation [39–40]. In this way, it may also be possible to tailor new MNWs to accommodate application-specific magnetic field strengths for optimal heating.

Theoretically, the area of a hysteresis loop determines the inductive loss of a magnetic material under AMF, or the specific loss power (SLP) in W/g. Therefore, the SLP for MNWs can be calculated using:

$$\mathrm{SLP} = \left(\int \mu_0 M dH\right) \cdot \frac{f}{\rho} \quad (2)$$

where $\mu_0 = 4\pi \times 10^{-7}$ H/m is the vacuum permeability, M in A/m is the magnetization of MNW at each applied field H in kA/m, f is the frequency of the AMF in Hz and ρ in kg/m^3 is the density of the material. The frequency was set to 50 kHz. The calculated SLP values for all MNWs studied in this paper are tabulated in Table 2. Hysteresis loops were also simulated for several MNWs at 300 kHz, the high end of magnetic heating frequencies, and the area was comparable to DC loops (±10%). Fernandez -Roldan et al. performed AMF simulation for MNWs and also showed that the hysteresis loop area difference between AC loops and a quasistatic loop only appears at very high frequencies (> MHz) [41]. This happens because the magnetization of MNWs reverses by the propagation of domain walls that nucleates at the MNW ends. The domain walls have enough time to fully reverse the magnetic moment in MNW up to MHz. This is an advantage of MNWs to SPIONs which rely on AC fields to open their otherwise zero-area hysteresis loops because their magnetization reverses by superparamagnetic coherent reversal [42]. Interestingly, as discussed above, the hysteresis loop of SPIONs is non-zero and not frequency dependent if the SPIONs form chains [19–21,42]. This serendipitous formation of chains is not easy to control whereas the geometry of MNW can be precisely engineered.

Table 2. Summary of theoretical specific loss power (SLP) for different materials and sizes studied. For typically available AMF systems (80 kA/m field limit), the optimal achievable SLP was achieved by Co MNW with 50 nm diameter (red). A frequency of 50 kHz was used for all calculations.

SLP [W/g] @ 50kHz	$D = 10$ nm	$D = 50$ nm	$D = 100$ nm	$D = 200$ nm
Co	78600	2730	890	249
Ni	19600	675	194	55
Fe	97300	2265	895	370
Py	49300	2215	620	172

From Table 2, we can conclude that Co MNWs with 50 nm diameter are the best candidate to use as a heat source among all the MNWs simulated in this study. Although theoretically, smaller (10 nm) MNWs can provide even better heating due to both large coercivities and only transverse domain walls form at reversal (Figure 4), the enormous fields required to switch these MNWs (more than 1000 kA/m) are well above the ability of typical AMF heater systems (80 kA/m field limit) [43].

Thus, we can consider how Co 50 nm MNWs will perform in the nanowarming of cryopreserved bio-samples, which is an interesting new application of nano-inductive loss. While it is true that Co is not as biocompatible as Fe, it has a similarly large moment, 1400 kA/m, and larger coercivity for the same size (see Figure 3). Therefore, Co is simulated to have a larger hysteresis loop area and thus better heating ability.

For applications like nanowarming cryopreserved organs, magnetic nanoparticles are only introduced to an organ or tissue during cooling. This means that metabolism is low, and immediately after melting, the nanoparticles are rinsed from the specimen. In addition, these MNW will be coated [44] for suspension in CPAs and for improved biocompatibility. Successful coatings have been innovated already to

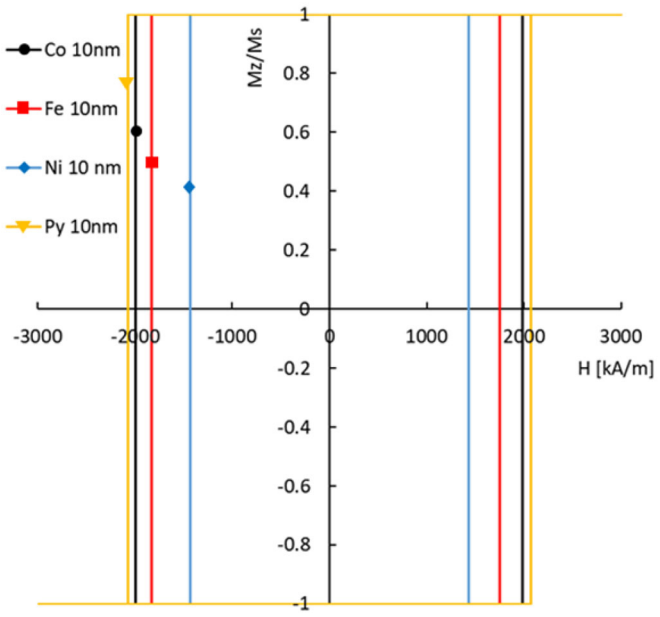

Figure 4. Hysteresis loops of Co (black with dot), Fe (red with square), Ni (blue with diamond), Py (yellow with a triangle) MNWs with small diameter (10 nm).

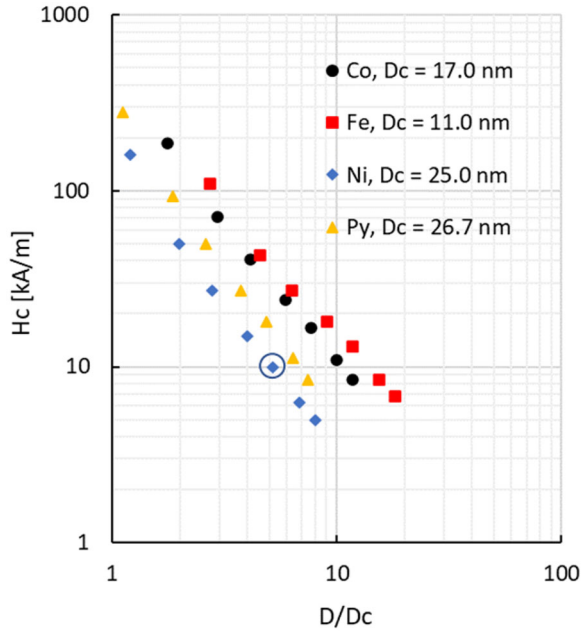

Figure 5. Correlation between the coercivity H_c in kA/m and the normalized diameter D/D_c for MNWs with different materials (black dot for Co, red square for Fe, blue diamond for Ni and yellow triangle for Py). Log axis is chosen to clearly show the $\sim D^{-2}$ relationship that is expected for VDW reversal [39].

improve the suspension and biocompatibility of SPIONs [45–47]. It should be noted that the Atkinson or Dutz-Hergt limit could restrain the total field frequency product for a patient receiving hyperthermia treatment. However, for the nanowarming processes presented here, a critical warming rate of 50 K/min is required and *ex vivo* organs have been successfully rewarmed using the field frequency products discussed above [14,48]. For future applications in hyperthermia treatment, MNWs may also prove valuable because high frequencies are not required for large hysteresis loops.

Two criteria are important in the application of nanowarming cryopreserved cells, tissues or organs. First, to avoid thermal damage to tissues and organs, such as large-scale cracks, uniform distribution of heating is required and could be easily achieved with these very small particles, either in cellular assays or throughout the vasculature of a cryopreserved organ. Second, to avoid de-vitrification of the CPA, the heating rate must exceed a critical warming rate, for example, 50 K/min for the popular VS55 cocktail [49]. The expected warming rate of Co 50 nm MNWs can be calculated from:

$$\begin{aligned}\text{Warming rate} &= \frac{\text{SLP}\cdot X}{C}\\ &= 2730\ \left[\frac{J}{g\cdot s}\right] \times 0.018\ \left[\frac{g}{ml}\right] \times \frac{1}{2.64\left[\frac{K\cdot ml}{J}\right]}\\ &= 18.63\ \frac{K}{s} = 1118\ \frac{K}{min}\end{aligned} \tag{3}$$

where C is the heat capacity of VS55 (2.64 J/(ml K) [50]), and X is the concentration of Co MNWs in the solution (18 mg MNW/ml of VS55). An estimated warming rate of 1118 K/min can be achieved, which is over 20× faster than the critical warming rate of VS55. A concentration of 100 mg/ml was required for SPIONs to heat 2× the critical warming rate of VS55 with extensive optimization. This result shows that MNWs have the potential to be extreme game changers in nano-heating applications.

More generally, the simulation results suggest a correlation between the coercivity and the intrinsic properties of MNWs such as size (represented by the normalized diameter) and material, which is shown in Figure 5. Based on this chart, we can easily find the required magnetic field strength of an AMF system to fully switch the MNWs. Or if we have a maximum available AMF field strength, we can decide what type of MNW to fabricate. For example, if an AMF can supply a maximum field strength of 10 kA/m, then we could choose Ni MNWs with diameters 5x the critical diameter (circled in Figure 5).

Conclusions

In conclusion, the general trend of isolated MNWs is that the coercivity and magnetic remanence inversely correlated to the diameter of the MWNs. From the calculated area, it is estimated that Co MNWs with 50 nm diameter are likely to be the best candidate for biomedical heating applications among all of the samples simulated in this study. These MNWs can provide theoretical heating of 2730 W/g within reasonable frequencies and fields of typical AMF heating systems. A theoretical warming rate of 1118 K/min is predicted for 18 mg MNW/ml VS55, which is 20x faster than the critical warming rate of VS55. Together with their small size which lends itself to a uniform distribution, these results suggest that Co 50 nm MNWs are excellent candidates for nanowarming cryopreserved cells, tissues, or organs.

Disclosure statement

No potential conflict of interest was reported by the author(s).

Funding

Partial support was provided by the ATP-Bio Engineering Research Center *via* NSF Award No. EEC-1941543 and the Air Force Office of Scientific Research Dr Ali Sayir *via* FA9550-21-1-0273. Part of the research was done in the UMN Characterization Facilities and the Minnesota Nanofabrication Center, both with partial support from NSF *via* MRSEC DMR-2011401 and NSF NNCI ECCS-2025124, and the Institute of Rock Magnetism (NSF EAR-1642268).

ORCID

Yicong Chen http://orcid.org/0000-0002-8987-9378
Bethanie J.H. Stadler http://orcid.org/0000-0002-3845-2833

Data availability statement

The data that support the findings of this study are openly available in Figshare at https://doi.org/10.6084/m9.figshare.22040795.v1.

References

[1] Fert A, Piraux L. Magnetic nanowires. J Magn Magn Mater. 1999; 200(1-3):338–358.
[2] Piraux L, George JM, Despres JF, et al. Giant magnetoresistance in magnetic multilayered nanowires. Appl Phys Lett. 1994;65(19): 2484–2486.
[3] Blondel A, Meier JP, Doudin B, et al. Giant magnetoresistance of nanowires of multilayers. Appl Phys Lett. 1994;65(23):3019–3021.
[4] Parkin SS, Hayashi M, Thomas L. Magnetic domain-wall racetrack memory. Science. 2008;320(5873):190–194.
[5] Shore D, Pailloux SL, Zhang J, et al. Electrodeposited Fe and Fe–Au nanowires as MRI contrast agents. Chem Commun. 2016; 52(85):12634–12637.
[6] Zamani Kouhpanji MR, Ghoreyshi A, Visscher PB, et al. Facile decoding of quantitative signatures from magnetic nanowire arrays. Sci Rep. 2020;10(1):1–9.
[7] Jeon YS, Shin HM, Kim YJ, et al. Metallic Fe–Au barcode nanowires as a simultaneous T cell capturing and cytokine sensing platform for immunoassay at the single-cell level. ACS Appl Mater Interfaces. 2019;11(27):23901–23908.
[8] Choi DS, Park J, Kim S, et al. Hyperthermia with magnetic nanowires for inactivating living cells. J Nanosci Nanotechnol. 2008; 8(5):2323–2327.
[9] Alonso J, Khurshid H, Sankar V, et al. FeCo nanowires with enhanced heating powers and controllable dimensions for magnetic hyperthermia. J Appl Phys. 2015;117(17):17D113.
[10] Egolf PW, Shamsudhin N, Pané S, et al. Hyperthermia with rotating magnetic nanowires inducing heat into tumor by fluid friction. J Appl Phys. 2016;120(6):064304.
[11] Gao Z, Namsrai B, Han Z, et al. Vitrification and rewarming of magnetic nanoparticle-loaded rat hearts. Adv Mat Technol. 2022; 7(3):2100873.
[12] Lin WS, Lin HM, Chen HH, et al. Shape effects of iron nanowires on hyperthermia treatment. J Nanomater. 2013;2013:1–6.
[13] Chen XZ, Hoop M, Mushtaq F, et al. Recent developments in magnetically driven micro-and nanorobots. Appl Mater Today. 2017;9:37–48.
[14] Sharma A, Rao JS, Han Z, et al. Vitrification and nanowarming of kidneys. Adv Sci. 2021;8(19):2101691.
[15] Lavorato GC, Das R, Masa JA, et al. Hybrid magnetic nanoparticles as efficient nanoheaters in biomedical applications. Nanoscale Adv. 2021;3(4):867–888.
[16] Di Corato R, Espinosa A, Lartigue L, et al. Magnetic hyperthermia efficiency in the cellular environment for different nanoparticle designs. Biomaterials. 2014;35(24):6400–6411.
[17] Geng S, Yang H, Ren X, et al. Anisotropic magnetite nanorods for enhanced magnetic hyperthermia. Chemistry–An. Chem Asian J. 2016;11(21):2996–3000.
[18] Martín-Saavedra FM, Ruíz-Hernández E, Boré A, et al. Magnetic mesoporous silica spheres for hyperthermia therapy. Acta Biomater. 2010;6(12):4522–4531.
[19] Serantes D, Baldomir D, Pereiro M, et al. Magnetic ordering in arrays of one-dimensional nanoparticle chains. J Phys D: Appl Phys. 2009;42(21):215003.
[20] Serantes D, Vega V, Rosa WD, et al. Interplay between magnetic anisotropy and dipolar interaction in one-dimensional nanomagnets: optimized magnetocaloric effect. Phys Rev B. 2012;86(10): 104431.
[21] Serantes D, Simeonidis K, Angelakeris M, et al. Multiplying magnetic hyperthermia response by nanoparticle assembling. J Phys Chem C. 2014;118(11):5927–5934.
[22] Das R, Alonso J, Nemati Porshokouh Z, et al. Tunable high aspect ratio iron oxide nanorods for enhanced hyperthermia. J Phys Chem C. 2016;120(18):10086–10093.
[23] Shore D, Ghemes A, Dragos-Pinzaru O, et al. Nanowarming using Au-tipped Co 35 Fe 65 ferromagnetic nanowires. Nanoscale. 2019;11(31):14607–14615.
[24] Sharma A, Orlowski GM, Zhu Y, et al. Inducing cells to disperse nickel nanowires via integrin-mediated responses. Nanotechnology. 2015; 26(13):135102.
[25] Carrey J, Mehdaoui B, Respaud M. Simple models for dynamic hysteresis loop calculations of magnetic single-domain nanoparticles: application to magnetic hyperthermia optimization. J Appl Phys. 2011;109(8):083921.
[26] Hubert A, Schäfer R. Domain theory. In: Magnetic domains. Berlin (Heidelberg): Springer; 1998. p. 99–335.
[27] Aharoni A, Arrott A. Introduction to the theory of ferromagnetism. Phys Today. 1997;50(9):66–68.
[28] Cullity BD, Graham CD. Introduction to magnetic materials. Hoboken (NJ): Wiley; 2008. Chapter 9, p. 275–333.
[29] Sampaio J, Cros V, Rohart S, et al. Nucleation, stability and current-induced motion of isolated magnetic skyrmions in nanostructures. Nat Nanotechnol. 2013;8(11):839–844.
[30] Woo S, Litzius K, Krüger B, et al. Observation of room-temperature magnetic skyrmions and their current-driven dynamics in ultrathin metallic ferromagnets. Nat Mater. 2016;15(5):501–506.
[31] Wartelle A, Trapp B, Staňo M, et al. Bloch-point-mediated topological transformations of magnetic domain walls in cylindrical nanowires. Phys Rev B. 2019;99(2):024433.
[32] Pignard S, Goglio G, Radulescu A, et al. Study of the magnetization reversal in individual nickel nanowires. J Appl Phys. 2000; 87(2):824–829.
[33] Mohammed H, Moreno JA, Kosel J. Advanced fabrication and characterization of magnetic nanowires. Magnetism Magnetic Mat. 2017;2:137–164.
[34] Donahue MJ, Porter DG. OOMMF user's guide version 1.0. National Institute of Standards and Technology; 1999. (Interagency Report NISTIR 6376).
[35] Beg M, Pepper RA, Fangohr H. User interfaces for computational science: a domain specific language for OOMMF embedded in python. AIP Adv. 2017;7(5):056025.
[36] Ivanov YP, Fesenko OC. Micromagnetic simulations of cylindrical magnetic nanowires. In: Magnetic Nano, and Microwires, Woodhead Publishing Series in Electronic and Optical Materials. Elsevier; 2015. p. 423–448.
[37] Sun L, Hao Y, Chien CL, et al. Tuning the properties of magnetic nanowires. IBM J Res & Dev. 2005;49(1):79–102.
[38] Huang J, Guo J, Zhou L, et al. Advanced nanomaterials-assisted cell cryopreservation: a mini review. ACS Appl Bio Mater. 2021; 4(4):2996–3014.
[39] Huysmans GT, Lodder JC, Wakui J. Magnetization curling in perpendicular iron particle arrays (alumite media). J Appl Phys. 1988; 64(4):2016–2021.

[40] Madhukar Reddy S, Jin Park J, Maqableh MM, et al. Magnetization reversal mechanisms in 35-nm diameter Fe1-x Ga x/Cu multilayered nanowires. J Appl Phys. 2012;111(7):07A920.
[41] Fernandez-Roldan JA, Serantes D, del Real RP, et al. Micromagnetic evaluation of the dissipated heat in cylindrical magnetic nanowires. Appl Phys Lett. 2018;112(21):212402.
[42] Rodrigo I, Castellanos-Rubio I, Garaio E, et al. Exploring the potential of the dynamic hysteresis loops via high field, high frequency and temperature adjustable AC magnetometer for magnetic hyperthermia characterization. Int J Hyperthermia. 2020;37(1):976–991.
[43] Zeinoun M, Serrano D, Medina PT, et al. Configurable high-frequency alternating magnetic field generator for nanomedical magnetic hyperthermia applications. IEEE Access. 2021;9:105805–105816.
[44] Nana AB, Marimuthu T, Kondiah PP, et al. Multifunctional magnetic nanowires: design, fabrication, and future prospects as cancer therapeutics. Cancers. 2019;11(12):1956.
[45] Jeon S, Oberreit DR, Van Schooneveld G, et al. Ion-mobility-based quantification of surface-coating-dependent binding of serum albumin to superparamagnetic iron oxide nanoparticles. ACS Appl Mater Interfaces. 2016;8(37):24482–24490.
[46] Gao Z, Ring HL, Sharma A, et al. Preparation of scalable silica-coated iron oxide nanoparticles for nanowarming. Adv Sci. 2020;7(4):1901624.
[47] Pasek-Allen JL, Wilharm RK, Gao Z, et al. Phosphonate coating of commercial iron oxide nanoparticles for nanowarming cryopreserved samples. J Mater Chem B. 2022;10(19):3734–3746.
[48] Chiu-Lam A, Staples E, Pepine CJ, et al. Perfusion, cryopreservation, and nanowarming of whole hearts using colloidally stable magnetic cryopreservation agent solutions. Sci Adv. 2021;7(2):eabe3005.
[49] Manuchehrabadi N, Gao Z, Zhang J, et al. Improved tissue cryopreservation using inductive heating of magnetic nanoparticles. Sci Transl Med. 2017;9(379):eaah4586.
[50] Eisenberg DP, Steif PS, Rabin Y. On the effects of thermal history on the development and relaxation of thermo-mechanical stress in cryopreservation. Cryogenics. 2014;64:86–94.